frontiers | Frontiers in Nanotechnology

TYPE Brief Research Report
PUBLISHED 04 September 2025
DOI 10.3389/fnano.2025.1597129

OPEN ACCESS

EDITED BY
B. H. Jaswanth Gowda,
Yenepoya University, India

REVIEWED BY
Prem Prakash,
Meharry Medical College, United States
Carlos Marcuello,
Spanish National Research Council (CSIC), Spain

*CORRESPONDENCE
Kristina Djanashvili,
k.djanashvili@tudelft.nl

RECEIVED 20 March 2025
ACCEPTED 25 August 2025
PUBLISHED 04 September 2025

CITATION
Van Oossanen R, Amaregouda M, Striekwold T, Maier A, Denkova AG, Godart J, Van Rhoon GC and Djanashvili K (2025) Exploring a spark-ablation setup for production of water-dispersed nanoparticles for biomedical applications.
Front. Nanotechnol. 7:1597129.
doi: 10.3389/fnano.2025.1597129

Exploring a spark-ablation setup for production of water-dispersed nanoparticles for biomedical applications

Rogier Van Oossanen[1,2], Meghana Amaregouda[2,3], Thijs Striekwold[2], Alexandra Maier[1,2], Antonia G. Denkova[2], Jérémy Godart[1], Gerard C. Van Rhoon[1,2] and Kristina Djanashvili[2,3]*

[1]Department of Radiotherapy, Erasmus MC Cancer Institute, University Medical Center, Rotterdam, Netherlands, [2]Department of Radiation Science and Technology, Delft University of Technology, Delft, Netherlands, [3]Department of Biotechnology, Delft University of Technology, Delft, Netherlands

The interest in hybrid nanoparticles for various applications in biomedicine is growing inevitably, stimulating research towards not only more effective, but also more accessible systems. This resulted in the emergence of advanced synthetic protocols with optimized conditions for the production of nanoparticles with high yields and desired morphologies, which ultimately determine their physicochemical and biomedical properties. While these challenges were sufficient for scientists a few decades ago, the sustainability of the synthetic methods is now an important aspect. From this perspective, nanoparticle production methods based on physical principles, such as spark discharge phenomena, could provide an interesting alternative to labor-intensive and environmentally harmful chemical synthesis. The benefits of clean and sustainable physical production routes for various nanomaterials are already recognized in the fields of catalysis and electronics. Biomedicine on the other hand has been reluctant to embrace the new methodologies, as they do not inherently provide nanoparticles dispersed in aqueous media, which is essential for their safe administration and reliable physiological performance. In this work, we investigated the potential of spark discharge as an alternative method to produce hybrid palladium/iron oxide nanoparticles intended for cancer thermo-brachytherapy by leveraging the magnetothermal properties of iron and the favorable radioactive features of the palladium radioisotope. Focusing on the aqueous harvesting of the nanoparticles produced in VSParticle's spark discharge generator, we determined the optimal settings compatible with the connected bubbling column and identified the pitfalls and possible solutions to the intrinsic challenges, such as low yields and aggregation.

KEYWORDS

physical synthetic methods, spark discharge, spark ablation, bubbling column, hybrid nanoparticles, iron oxide, palladium, citric acid

1 Introduction

Nanomaterials are rapidly making inroads into the biomedical field due to their unique nanoscale properties and unprecedented effects on biological systems. Nanomedicine exploits these phenomena by translating them into innovative therapeutic and diagnostic tools for the detection and treatment of various diseases. This complex interplay between materials science and medicine is driving research into smart nanomaterials, with objectives focused on the facile, clean, and reproducible synthetic routes (Starsich et al., 2019). Reflecting this demand, the global nanomedicine market is currently valued at approximately USD 200 billion and, with annual growth rates of 11%–12%, is projected to exceed USD 450 billion within the next decade (Credence Research; Grand View Research).

Iron oxide nanoparticles (IONs), typically in the form of magnetite (Fe_3O_4) and/or maghemite (γ-Fe_2O_3), are highly functional materials, whose size-dependent physicochemical and magnetic properties render them valuable in cancer diagnosis and therapy. In magnetic resonance imaging (MRI), superparamagnetic IONs (10–30 nm) act as T_2 contrast agents by enhancing transverse relaxation rates via efficient proton spin dephasing controlled by saturation magnetization and magnetic anisotropy, along with particle size (Vangijzegem et al., 2023; Wi et al., 2023). Furthermore, IONs are biocompatible, and their surface is easily functionalized, making them ideal for precise and controlled drug delivery (Stanicki et al., 2022; Ghazi et al., 2025), which can be achieved through external-field-guided targeting, site-specific retention, and even magnetically triggered release. Beyond imaging and drug delivery, IONs find use in magnetic hyperthermia/thermal ablation, where exposure to alternating magnetic fields generates localized heating (Laurent et al., 2011). Again, efficiency depends on magnetic properties of IONs dictated by their size and composition. Such tunability is particularly important in multimodal facets, where iron is mixed with other metals, such as luminescent lanthanides (Laha et al., 2022) or radioisotopes (Pellico et al., 2023).

Most synthetic procedures developed over recent decades for metal NPs in general and iron oxide NPs in particular, rely on wet chemistry techniques (Fortin et al., 2007; Nemati et al., 2018). Methods such as co-precipitation, thermal decomposition, micro-emulsion, and sol-gel can be effective, but pose challenges in producing NPs with consistent characteristics essential for biomedical applications, including good colloidal stability and monodispersity. These challenges become even more pronounced in the case of hybrid NPs, as the presence of multiple constituent elements can lead to heterogeneous surface chemistry, resulting in uneven charge distribution, reduced electrostatic repulsion between NPs, and subsequent aggregation (Nedylakova et al., 2024). Physical methods for NPs synthesis offer an interesting alternative; yet, despite their widespread use in catalysis and electronics, they remain notably underutilized in nanomedicine.

One of the physical synthetic methods that could provide consistency in the physicochemical properties of certain NPs is the environmentally friendly spark discharge technology (Tabrizi et al., 2009). The essence of the method is that two metal electrodes are placed ±1 mm apart, and then, a high voltage is applied, causing an electrical discharge across the gap between the two electrodes. The transient current created locally, heats the electrodes up to 30,000 K, resulting in spark ablation and evaporation of a small amount of metal from the surface. The continuous gas flow carries the vapor with it, allowing the atoms to cool and collide to form NPs (Schwyn et al., 1988). After over 25 years of use, spark ablation has become an established commercial technique for generating gas-borne aerosols or surface-deposited NPs, primarily in industrial settings. We see strong potential of this technology for medicine, particularly due to the great advantage in producing hybrid NPs by combining electrodes of different metals. This method also enables the creation of diverse topologies such as core-shell or alloy NPs, by selecting appropriate electrode materials. However, to translate these nanomaterials into biomedical use, it is essential to harvest them in aqueous media to ensure biocompatibility, stability, and dispersibility in physiological environments, as well as to facilitate biomolecular functionalization. Preventing aggregation–often a challenge in physically synthesized materials–is also crucial, as it otherwise limits their biomedical effectiveness.

Previously, we reported the chemical synthesis of palladium/iron oxide nanoparticles (Pd/Fe-oxide NPs) designed for cancer imaging and therapy (Maier et al., 2021). Seeking an alternative, more straightforward route to obtain these NPs directly in aqueous media, eliminating the need for additional surfactant exchange steps, we investigated the use of a spark discharge generator (SDG) in combination with a bubbling column as a receiver of gas-borne NPs produced by SDG–a setup, to the best of our knowledge not yet described. Furthermore, we systematically examined the influence of key process parameters based, including gas flow rates, bubble size, liquid properties and spark generation conditions, on the efficiency and effectiveness of nanoparticle collection, taking into account available theoretical models related to these parameters.

2 Materials and methods

2.1 Experimental setup and underlying physical mechanisms

Production of NPs was carried out with the VSP-G1 commercial spark discharge device (VSParticle, Netherlands) operating in accordance with the principles proposed and described by Burtscher and Schmidt-Ott (1982). This device comprises a sealed reactor chamber containing a pair of opposing metallic electrodes (anode and cathode) and an in(out)let nozzle that admits an inert gas into the inter-electrode gap. A high-power DC (direct current) source intermittently charges a shunted capacitor, generating a substantial voltage difference across the electrodes. Once the capacitor reaches its breakdown voltage, which depends on the gas pressure and the distance between electrodes (Mathew et al., 2019), the gaseous dielectric medium becomes conductive. This allows electrons and positive ions to migrate toward electrodes of opposite polarity. Due to their much higher mobility, electrons rapidly move forward and are absorbed by the anode. In contrast, the more massive positive ions strike the cathode, triggering secondary electron emissions. This initiates a self-sustaining plasma channel between the electrodes, where the resulting high current discharge arc can reach extreme temperatures of 20,000–30,000 K (Reinmann and Akram, 1997). This thermal energy applied over a small area,

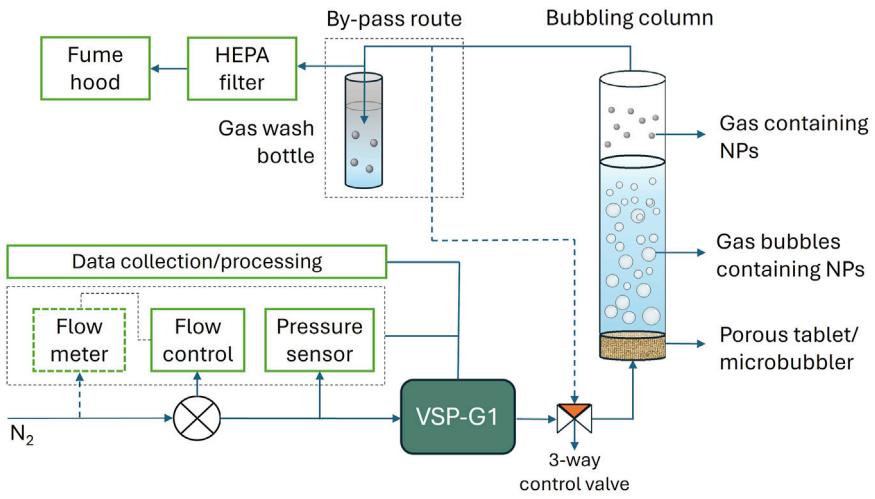

FIGURE 1
Experimental setup of the VSP-G1 spark discharge device combined with a bubbling column.

triggers evaporation of electrode material after being heated far above its boiling point. Although more material is eroded from the cathode than from the anode due to the positive ion bombardment at the start of discharge, the damping behavior of spark lowers the contribution from the anode. The plasma plume containing the species of the inert gas and the electrode material is released between the electrodes and in the vicinity of the electrode setup. This adiabatic expansion and diffusion results in the condensation of metal vapor when mixed with the surrounding inert gas. The condensation is followed by clustering, nucleation, and growth of NPs (Pfeiffer et al., 2014) carried by the inert gas from the system to a collection point, which in this study was a bubbling column.

Nitrogen (N_2) was used as a carrier gas with flow rates varying between 0.5 and 3 L/min, regulated by an EL-FLOW Base F-201CB three-way electronic control valve (Brockhorst, Netherlands) to inhibit backflow of water from the bubbling column into the generator. When the valve was closed, the nanoparticles-laden gas was redirected through a by-pass line directly into the gas wash. The setup was used under atmospheric pressure, with a safety system installed to stop the gas at a pressure higher than 1.4 mbar. The electrodes, made of iron (Fe, 99.99%) and palladium (Pd, 99.99%), were aligned orthogonally relative to the gas flow. The applied spark voltage and current ranged from 0.7 to 1.3 kV and 2.5–10 mA, respectively. A glass bubbling column filled with Milli-Q water was equipped with a compacted and sintered bronze disc with a pore size <20 µm. Passing the column, the gas containing non-retained NPs was directed into the ventilation system through a wash-bottle and a HEPA filter (Figure 1).

2.2 Characterization methods

The hydrodynamic radius of the NPs was determined with dynamic light scattering (DLS) method using a setup, which consisted of a 633 nm/35 mW JDS Uniphase (United States) in combination with a sp-125/w-93 goniometer (ALV, Germany) and a photo-counter (Perkin Elmer, United States). The data were analyzed using the CONTIN method. For the analysis, a 2 mL sample was taken from the column, possible agglomerates were removed using a 400 nm membrane filter, and the sample was diluted until the measured frequency was below 1 MHz. TEM images were acquired on a 120 kV JEM1400 microscope (JEOL, Japan) with 0.1–0.5 µL of the sample placed on an R1.2/1.3 Cu 300 grid (Quantifoil, Germany), which allowed to dry first at room temperature. The mean diameter and the size distribution of the samples were determined by statistical analysis over 500–1,000 NPs with ImageJ software. Scanning electron microscopy with energy dispersive X-ray spectroscopy (SEM/EDX) was performed with a JSM-IT100 device (JEOL, Japan). The sample was prepared by drying a 0.5 mL droplet on a carbon tape. Initially, SED of 7 kV and HV of ×40 were used with higher values applied if the count rate fell below 1,000 cps. The EDX measurements were performed for 1.5 h. Inductively coupled plasma optical emission spectroscopy (ICP-OES) was performed with an Optima 5300 (Perkin Elmer, United States) spectrometer to determine the elemental analysis of the NPs using the ICP-OES 5300DV software. Prior to the measurement, the NPs were digested by addition of 1.5 mL of nitric acid per 10 mL of the sample and subjected to additional microwave heating in the case of Pd-containing NPs. The calibration lines were constructed using standard Fe- and Pd-solutions (Sigma-Aldrich). The crystalline structure of the NPs was evaluated by X-ray diffraction analysis (XRD) carried out on a PANalytical XPERT-PRO diffractometer (Malvern Panalytical, United Kingdom) set at 45 kV and 40 mA with a copper X-ray tube. A monochromator was used to avoid fluorescence of iron in the sample when exposed to copper X-rays; the measurement angles ranged from 10° to 90°. Transmission ^{57}Fe Mössbauer data were obtained at 300 K with a constant-acceleration spectrometer using a ^{57}Co(Rh) source. The data were analyzed using Mosswinn software (Klencsár, 1997). Mass magnetization was measured with a Quantum Design Versalab VSM (vibrating sample magnetometer) device operating at a magnetic field up to 3T generated by 20A current. The nano-powders were demagnetized with De-Gauss under simultaneous application of an opposing magnetic field at 300 K.

3 Results and discussion

3.1 Establishment of experimental settings

Metal mixing was achieved by combining iron and palladium electrodes, while NP accumulation in water was realized based on their entrainment in buoyant bubbles ascending through a water-filled column. This special experimental setup required optimization of the settings involved in NP production, including three key parameters: (A) gas-related factors, (B) electrode settings, and (C) bubbling column size.

3.1.1 Gas-related parameters

The optimization of the experimental setup started with considerations of gas-related parameters, such as gas types, flow rates, etc. These parameters are known to affect the composition, morphology, and size of the NPs, and as such, are described in detail for conventional spark-ablation systems (Tabrizi et al., 2009). For example, H_2 leads to hydride metallic/metal oxide NPs, O_2 provides the NPs with an oxidative layer, while inert gasses, such as N_2 and Ar, initially yield pure metallic NPs. However, the primary role of gas in the SDG process is rapid cooling (quenching) of the atomic plasma, which initiates formation of atomic clusters. Once the clusters reach a critical size, the nucleation process sets in, driven by the system's thermodynamically unfavorable positive free energy resulting from high surface energy. Each metal has a distinct critical cluster size, which along with the number of atomic clusters and their proximity, temperature and cooling rate, determines the final NPs size. Naturally, elevated gas flow increases the cooling rate of NPs and decreases the contact time between the clusters, which results in smaller particles (1–10 nm) (Maisser et al., 2015).

The thermal conductivity (k) of the carrier gas is another important factor because it influences charge formation, and thus affects the efficiency of thermal energy transfer to the electrodes, leading to increased electrode material ablation. This explains why primary particles formed in the presence of nitrogen as the quenching gas ($k = 2.59 \times 10^{-2}$ W m^{-1}K^{-1}) tend to be larger than those produced in argon ($k = 1.77 \times 10^{-2}$ W m^{-1}K^{-1}). Additionally, nitrogen's shorter mean free path increases the likelihood of collision between NPs and gas molecules, thereby enhancing the cooling rate, and consequently the particle size (Tabrizi et al., 2009; Tabrizi et al., 2010). This process is strongly influenced by the flow rate of the carrier gas resulting in larger NPs up to 5 L/min, above which the size of NPs becomes independent of the flow rate (Feng et al., 2016). Aiming at relatively large NPs (±20 nm diameter), the flow rates were initially varied from 0.5 to 3 L/min. However, we noted that the presence of a bubbling column as part of the set-up instead of the conventional NPs deposition unit, complicated the process by excessive build-up of ablated material inside the reactor chamber under insufficient flow.

3.1.2 Electrode settings

The optimal NPs yield was approached taking into account the observation of moderate voltage and maximum current resulting in higher production rate. Since a rather low voltage (0.65 kV) caused fluctuation in sparking due to insufficient flush out of charges at high frequency, the final settings applied were 1.3 kV and 10 mA in combination with N_2 flow of 2 L/min.

Moreover, the use of two different electrodes for generation of hybrid NPs involves the choice of an element that serves either as an anode or cathode. The discharge current exhibits an oscillatory behavior due to the characteristics of the RLC circuit, which drives the vaporization of the electrode material. Both electrodes undergo significant ablation, with the extent depending on the polarity of the oscillating current, ultimately leading to the formation of internally mixed NPs. For reasons explained earlier, the cathode is usually subject to greater ablation than the anode, leading to a disproportionately large difference in the material consumption of the two electrodes. Since the intended theranostic application of the hybrid NPs requires strong magnetic properties, and hence a higher iron content, the iron electrode was used as cathode.

3.1.3 Bubbling column

The majority of the existing data on gas bubbling in the presence of NPs relates to gas purification rather than capturing NPs in water. Despite the different objectives, the underlying physical principles are sufficiently similar to support the development of a model for extraction efficiency, which serves as the foundation for the bubbling column investigated in our laboratory (Klencsár, 1997). The efficiency of NP deposition in a column filled with deionized water (or other aqueous media) relies on both absorption/diffusion processes and the column height (Koch and Weber, 2012), as described by Equation 1:

$$C_p = C_0 e^{-ah} \tag{1}$$

where C_p represents the concentration of NPs within the gas bubble, while C_0 denotes the NP concentration at the inlet of the bubbling column, parameter a is the absorption coefficient, and h is the height of the liquid column. The adsorption coefficient a, in turn, is a function of the diffusion coefficient D, the bubble rise velocity U_b and the radius r of an individual aerosol bubble, as defined by Equation 2:

$$a = 1.8\sqrt{\frac{D}{U_b r^3}} \tag{2}$$

Based on these equations, the key parameters influencing efficiency are the height of the bubbling column and the bubble radius, which directly reflects the gas flow rate and the viscosity of the surrounding medium. Intuitively, increasing the amount of water should lengthen the path for the bubbles to travel through the column and increase the retention of NPs. However, doubling the amount of water did not change the NPs yield significantly, and the iron content obtained by ICP-OES analysis for the aqueous phase of both the 100- and 200-mL columns fluctuated around 5 ± 1.5 mg/mL. On the contrary, a decrease in volume to 60 mL resulted in a higher iron concentration. This suggests that NPs diffusion from the bubbles into the water primarily takes place in the low section of the bubbling column, and that increasing the liquid volume mainly results in dilution rather than enhanced capture.

3.2 Effect of microbubble generation

Other factors that determine the diffusion rate of NPs from gas to water include the size of the bubbles and their rise rate, both of

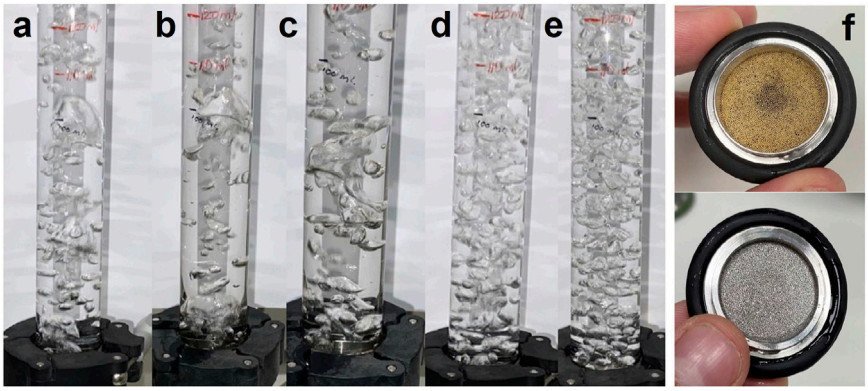

FIGURE 2
Bubble formation in the column filled with 100 mL of water at a flow rate of 1 L/min using various tablets: **(a)** metal mesh with small pores, **(b)** metal mesh with large pores, **(c)** four metal mesh with large pores stacked, **(d)** stainless steel porous tablet with pore size ±20 μm, **(e)** bronze porous tablet with pore size <20 μm, and **(f)** visual appearance of bronze (top) and stainless-steel (bottom) porous tablets.

which can be controlled by the gas flow. At higher flow rates, the bubble radius increases, decreasing the surface/volume ratio, which in turn reduces diffusion. However, it has been found that the absorption efficiency in the bubbling column can actually increase at high flow rates, if microbubbles are formed (Cadavid-Rodriguez et al., 2014). These microbubbles have a high surface-to-volume ratio, which compensates for the reduced ratio resulting from the turbulent flow.

The microbubble generation depends on the interplay between the gas flow and the aperture size of the porous tablet, which again emphasizes the importance of a low gas flow rate for smaller bubbles, enabling larger NPs and increasing the capture efficiency of the bubbling column (Gaddis and Vogelpohl, 1986). In addition, high flow rates ensure high material carryover from the generator. To address this, a porous tablet was positioned at the entrance to the water column to disperse gas through tiny holes. This setup allows gas to flow through in small bubbles, while preventing the water in the column from flowing out.

Different tablets were investigated and compared to find the possibility of creating small bubbles without causing pressure build-up, keeping in mind that SDG is not designed to operate >1.4 mbar (Figures 2a–e). First, a metal mesh KF25 filter with pores of 25 μm (a) was used resulting in big bubbles and a pressure built-up. The latter issue was solved with a mash with the pores as big as 300 μm (b), but the bubble formation deteriorated. Stacking four of these tablets (c) reduced the size of the bubbles, but did not increase the concentration of NPs in the water column and caused pressure built-up in the system instead. Furthermore, inspection of the tablets revealed that four mashes accumulated a large amount of material that never reached the water column. Finally, stainless steel (d) and sintered bronze (e) tablets with pore sizes of around 20 and below 20 μm, respectively, were investigated. Both porous tablets generated numerous small bubbles, enhancing capture efficiency within the bubbling column. A major drawback noted with the stainless-steel tablet was the built-up of material after 3 h of production time, resulting in a pressure increase by approximately 1.5 mbar. The bronze tablet performed much better in this regard: even after 5 days of operation, no pressure rise was observed, while the much higher throughput of NPs was maintained. Despite having a smaller pore size, the sintered bronze tablet appears to exhibit greater permeability than the sintered stainless-steel tablet (Figure 2f).

3.3 Synthesis and characterization of hybrid nanoparticles

The biggest advantage of spark technology over chemical synthesis is the ability to generate numerous types of NPs without the need to alter design and components except for the electrode material. Therefore, before venturing into the synthesis of Pd/Fe-oxide hybrid NPs, pure Pd- and Fe-NPs were first produced using the optimized settings described above to gain insight into their behavior in combination with bubbling column.

It was observed that most of the Pd-NPs produced during the experiment adhered to the glass surface of the bubbling column and a large amount of deposition was found on the porous tablet, while the remaining NPs suspended in Milli-Q water appeared as large aggregates. Assuming that this behavior was caused by the charge developed on the surface of PdO, the same experiment was conducted to generate Fe-NPs, but no deposition was observed. An explanation of this phenomenon can be found by examining the isoelectric point (IEP) of PdO (Didillon et al., 1998), which is 4.5, indicating a higher negative zeta-potential when suspended in Milli-Q water at neutral pH. The NPs were transported toward the glass wall by the continuous agitation of the suspension caused by bubbles and glass flow through the column, where they remained due to electrostatic interaction. This phenomenon was not encountered for Fe-NPs, due to the IEP of iron oxide of 6.8 (Fortin et al., 2007). The surface charge of Pd-NPs could be neutralized by lowering the pH in the water column down to 4.5-5 with HCl prior to the NPs generation experiment, which effectively stopped the glass adhesion. Consequently, even though the DLS measurements showed an aggregation with time (Supplementary Figure S1a), the original diameter of 4 nm for Pd-NPs was determined by TEM (Figure 3a).

As the result, the NPs were harvested in water with an apparent tendency to aggregate in time going from the initial size of 5 nm–70 nm and even above 1,000 (Figure 3b, Supplementary

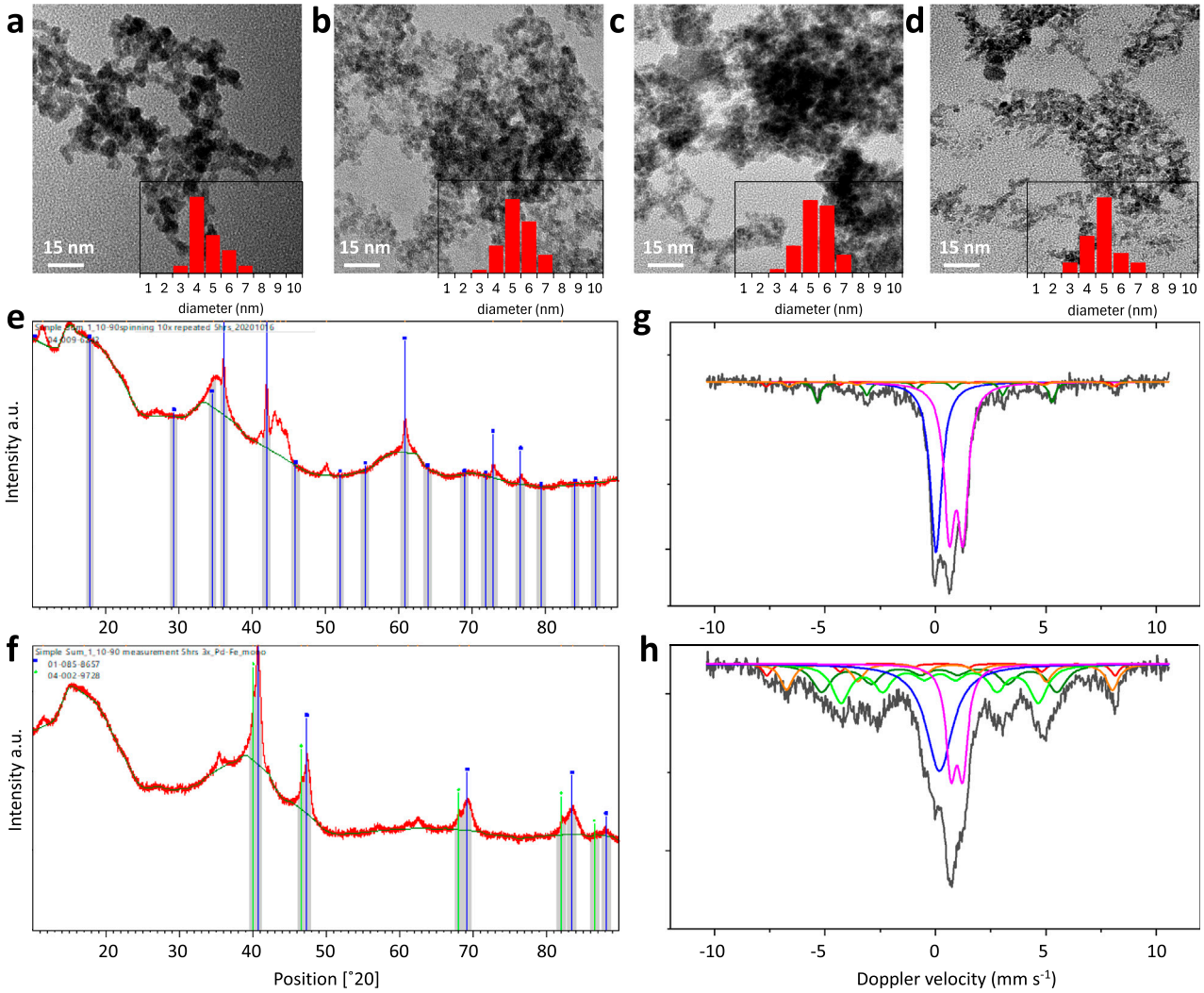

FIGURE 3
TEM images and size distributions of NPs prepared with VSP-G1 SDG operating at a voltage of 1.3 kV, a current of 10 mA and a N_2 flow of 2 L/min. Single electrodes were used for: palladium, producing Pd-NPs **(a)**, and iron, for Fe-oxide NPs **(b)**, mixed electrodes of palladium (anode) and iron (cathode) yielded Pd/Fe-oxide NPs, harvested in water **(c)**, or in a solution of 25 mM citric acid **(d)**. Insets show statistical size distribution determined from measurements of 500–1,000 NPs. The composition of Fe-oxide (top) and Pd/Fe-oxide (bottom) NPs was investigated by XRD **(e,f)** and Mössbauer spectroscopies **(g,h)**.

Figure S1b). Redispersion of three samples with aggregated NPs was attempted through a typically applied (ultra)sonication and monitored by DLS. Two samples were ultra-sonicated at a frequency of 20 kHz using an Ultrasonic Processor (Cole Parmer) with a 750 W sonicator probe at 20% amplitude and 27 °C for 3–5 min and one sample was sonicated with a conventional ultrasound bath (300 W). Interestingly, all three samples exhibited increased aggregation upon sonication, with the most pronounced effect observed for the ultra-sonicated samples, ultimately leading to material sedimentation. This increase in aggregation might be supported by the Derjaguin-Landau-Verwey-Overbeek (DLVO) theory (Walter et al., 2015), which connects the tendency of interacting NPs to aggregate with their potential energy. This energy is a combination of attractive van der Waals forces, repulsive electrical double-layer forces, and the generally neglectable solvent potential. The negatively charged surface of 'naked' iron oxide NPs typically causes them to repel each other. However, it is possible that NPs gain sufficient energy to partially overcome this repulsion, resulting in aggregation driven by increased van der Waals attraction. Ultra-sonication clearly introduces additional energy, which likely increases the probability of NPs overcoming the electrostatic repulsion and forming aggregates. This emphasizes the importance of a sufficient particle separation (r) between the NPs for the repulsive electrical double-layer force (U_R), following from Equation 3:

$$U_R = 2\pi\varepsilon\zeta^2 \exp(-kr) \quad (3)$$

where ε is the dielectric constant of the medium, ζ is the zeta potential, and k is a parameter related to the ionic strength. Moreover, the IEP of iron oxide, being close to the pH of the

Milli-Q water, contributed to the aggregation process. Lowering the pH could potentially lead to the dissolution of iron oxide and adding surfactants was ruled out due to the possible foam formation in the bubbling column. Therefore, in the case of Pd/Fe-oxide NPs, weak and biocompatible citric acid (CA) was considered a suitable choice to minimize foaming, while inducing the hydrophilic nature into the colloid.

The CA-coating procedures described for stabilization of chemically prepared iron oxide NPs (Dheyab et al., 2020) were adopted to the SDG production of the hybrid Pd/Fe-oxide NPs. Briefly, the bubbling column was filled with a 25 mM solution of CA which captured the incoming NPs. The results were compared to those of the procedure using a water-filled bubbling column, and the first observation made was an apparent decrease in the size of the bubbles (Supplementary Figure S2a,b). This in turn translated into a significant prevention of aggregation (Figures 3c,d, Supplementary Figure S1c,d) and an increased concentration of NPs in the column (Supplementary Figure S2c). The ICP-OES measurements on the NPs suspensions originating from the bubbling column revealed that the concentration of Pd/Fe-oxide NPs in the presence of CA were 5 times higher compared to their concentration without CA (Supplementary Table S1).

At room temperature, the density of a 1M aqueous solution of CA is 1.1 g/cm^3 and its viscosity is about 1 mPa·s. In comparison, the density and viscosity of water are 1 g/cm^3 and 0.9 mPa·s (Simion et al., 2014). A quantitative estimation of the dependence of the bubble radius (r) on the density (ρ), viscosity (ν) and surface tension (σ_t) can be done with Equation 4 (Gaddis and Vogelpohl, 1986):

$$r = 0.5\left[\left(\frac{6O_d\sigma_t}{\rho g}\right)^{\frac{4}{3}} + \left(\frac{81\nu Q}{\pi g}\right) + \left(\frac{135Q^2}{4\pi^2 g}\right)^{\frac{4}{5}}\right]^{\frac{1}{4}} \quad (4)$$

where O_d is the orifice diameter related to the pore size of the bronze tablet (<20 μm), Q is the flow rate, and g is bubble acceleration due to gravity. Since both the density and viscosity in the CA-column do not change to a large extent, they cannot be considered as the cause of the decrease in bubble size. Surface tension, on the other hand, plays a major role, as it goes down upon addition of CA and reduces the bubble coalescence frequency. Consequently, the bubbles were smaller, slower-moving and more rounded, leading to a higher concentration of CA-coated Pd/Fe-oxide NPs in the column. Moreover, the negatively charged carboxylate groups on the NP surface impart hydrophilicity, and the overall negative zeta-potential of the suspension contributed to its improved stability resulting in hardly any deposition of NPs on either porous tablet or on a 0.4 μm filter (Supplementary Figure S3).

Although the NP concentration in the bubbling column could be increased using CA, the low overall yields limited the investigation of the NP composition. As a result, the background signal in the XRD profiles of both Fe- and Pd/Fe-oxide NPs obtained from the bubbling column via freeze-drying was too high (Figures 3e,f). While fitting the seemingly different profiles with database structures of the corresponding materials revealed the characteristics peaks (Supplementary Table S2) in agreement with our previously reported work (Maier et al., 2024), no well-defined crystal structural information could be derived from the data. This is also consistent with the reported difficulties in identifying the small crystalline domains for the particles prepared by the spark discharge method, where they often approach the amorphous limit, resulting in significant broadening or even absence of characteristic peaks (Drdova et al., 2024).

The Mössbauer data were fitted with contributions from several iron-containing species: magnetite ($Fe^{2+}Fe_2^{3+}O_4$), which accounts for ferromagnetic behavior (5%); an intermediate reduced Fe^{2+} species (e.g., wüstite-FeO), which exhibits paramagnetism and metallic Fe-bulk structures (10%); and a small superparamagnetic species (34%). Details of the fit are provided in Table 1. In Figures 2g,h, the ferromagnetic spectral composition (green and yellow) is represented by the sextets, while the contribution of superparamagnetic particles is indicated by the doublet in the spectrum (pink). As previously observed for $Fe_{1-x}Pd_x$ alloys (Zhang and Zhang, 1994), compositions with $x < 0.6$ and $x > 0.85$ typically correspond to dominant ferromagnetic and paramagnetic behavior, respectively. This relationship cannot be directly translated to the Pd/Fe-oxide NPs in this study, as neither the Pd/Fe-ratios nor the crystal structures of the NPs are well-defined, unlike those of previously reported Pd/Fe-oxide NPs prepared via the thermal decomposition method (Maier et al., 2022).

Magnetization measurements of SDG-prepared NPs, conducted using a vibrating sample magnetometer, revealed relatively low magnetization (±20 emu/g, Supplementary Figure S4), which can be attributed not only to the small size, but also to the lack of well-ordered crystalline domains, which limits the development of high magnetocrystalline anisotropy. These physical and magnetic characteristics indicate a reduced magnetothermal response compared to previously reported chemically prepared Pd/Fe-oxide (Maier et al., 2022) and Pd|Mn/Fe-oxide (Maier et al., 2024) NPs. However, the observation that 25% of Pd/Fe alloy exhibits superparamagnetic properties, while 18% is paramagnetic suggests that generating magnetically responsive hybrid NPs is feasible.

4 Conclusion

In this work we investigated the feasibility of synthesizing metallic NPs using a spark discharge generator, demonstrated for Pd/Fe-oxide hybrid NPs. The focus of this study was on two aspects of primary importance in the development of NPs for biomedical applications: (1) the effect of instrument settings on NPs production, including their morphology and (2) the possibility of collecting the resulting NPs in aqueous media via a bubbling column with the yield required for an optimal magnetic performance.

Our findings demonstrate that the nanoparticle yield in the SDG-bubbling column setup is strongly influenced by key operational parameters. The observed increase in yield at higher voltages supports the theoretical expectation that nanoparticles production raises with the energy dissipated per spark. To balance both efficient yield and system stability, optimal voltage and current settings were identified, taking into account voltage fluctuations at higher frequencies. Additionally, an intermediate nitrogen flow rate was found to be most effective, as low flow rates led to increased nanoparticle retention within the generator, while excessively high rates resulted in larger bubbles, reducing diffusion and collection efficiency. The incorporation of a bronze tablet with fine pores further improved the process by producing small, uniform

TABLE 1 Mössbauer fitted parameters of the Fe-oxide and Pd/Fe-oxide NPs.

Sample	IS (mm s^{-1})	QS (mm s^{-1})	Hyperfine field (T)	Γ (mm s^{-1})	Phase	Spectral contribution (%)
Fe-oxide	0.02	-	-	0.63	Fe^0 (SPM)[a]	34
	0.00	-	33.0	0.37	Fe^0	10
	0.94	0.62	-	0.57	Fe^{2+}	51
	0.25	0.01	49.1	0.30	Fe^{2+} (Fe_3O_4, A)	2
	0.69	0.00	45.5	0.45	$Fe^{2.5}$ (Fe_3O_4, B)	3
Pd/Fe-oxide	0.18	-	-	1.46	Pd/Fe alloy[b] (SPM)	25
	0.18	-	33.1	1.00	Pd/Fe alloy[c]	18
	0.20	-	27.8	0.97	Pd/Fe alloy[d]	24
	0.97	0.53	-	0.55	Fe^{2+}	18
	0.25	0.01	49.0	0.45	Fe^{2+} (Fe_3O_4, A)	4
	0.69	−0.10	45.9	0.66	$Fe^{2.5}$ (Fe_3O_4, B)	11

Experimental uncertainties: Isomer shift (IS): ±0.02 mm s^{-1}; Quadrupole splitting (QS): ±0.02 mm s^{-1}; Line width: (Γ) ± 0.03 mm s^{-1}; Hyperfine field: ±0.1T; Spectral contribution: ±3%; [a]very small structures (<15 nm) superparamagnetic at RT; [b,c,d]Fe/Pd alloys with various Fe/Pd ratios.

bubbles that created favorable microenvironments for nanoparticle stabilization and efficient transfer into the aqueous phase.

The primary size of NPs produced by spark discharge at electrodes largely depends on the thermal properties of the corresponding element. For palladium, higher boiling and melting points, as well as higher vaporization and fusion enthalpies compared to iron, lead to a slightly smaller average size of Pd-NPs. However, these NPs tend to form large agglomerates in water due to their negative surface charge. Such behavior was not observed for pure Fe-oxide NPs, whereas in hybrid Pd/Fe-oxide systems, increased Pd content seemed to promote agglomeration. This drawback was effectively overcome by adding citric acid, which acted as a non-foaming surfactant and at the same time increased the yield from 0.5 to 2.5 mM. DLS measurements of CA-coated NPs harvested from the bubbling column showed narrow size distributions, consistent with the TEM images. The resulting mass magnetization of Pd/Fe-oxide NPs was on the low side, in agreement with their small size.

In summary, these findings highlight both the promising and limiting aspects of SDG-based production of NPs for biomedical applications. We showed that combining electrodes enables the synthesis of hybrid NPs and established optimal parameters and methods to suppress aggregation and improve NPs capture. As such, this investigation provides a reliable starting point for the aqueous-phase production and collection of metallic nanoparticles. However, the use of the bubbling column remains a major challenge associated with limitations in the applied flows and, as a result, increased material retention in the generator and, consequently, low yields. Therefore, further work should include comprehensive efforts for hardware modifications along with optimization of the NPs harvesting process. Furthermore, the low magnetization of the obtained NPs poses a challenge to achieving the heating performance thresholds required for therapeutic efficacy. This limitation can potentially be overcome through post-synthetic crystallization, such as final annealing treatments, which can promote grain growth and phase ordering in hybrid Fe-oxide NPs, thereby enhancing magnetocrystalline anisotropy and overall magnetic performance, or through compositional modifications.

Data availability statement

The original contributions presented in the study are included in the article/Supplementary Material, further inquiries can be directed to the corresponding author.

Author contributions

RO: Investigation, Methodology, Writing – original draft, Writing – review and editing. MA: Investigation, Methodology, Writing – original draft, Writing – review and editing. TS: Investigation, Methodology, Writing – original draft, Writing – review and editing. AM: Investigation, Methodology, Writing – original draft, Writing – review and editing. AD: Funding acquisition, Conceptualization, Supervision, Writing – original draft, Writing – review and editing. JG: Conceptualization, Supervision, Writing – original draft, Writing – review and editing. GR: Funding acquisition, Conceptualization, Supervision, Writing – original draft, Writing – review and editing. KD: Funding acquisition, Conceptualization, Validation, Supervision, Writing – original draft, Writing – review and editing.

Funding

The author(s) declare that financial support was received for the research and/or publication of this article. The research was supported by HTSM (High Tech Systemen en Materialen), a research program within the Dutch Research Council (NWO), Domain Applied and Engineering Sciences (AES), grant number 16238 and European Metrology Programme for Innovation and Research (Funder ID: 10.13039/100014132; grant number: 18HLT06 RaCHy).

Acknowledgments

The authors thank VSParticle for the fruitful discussions, and in particular, Sofia Dimitriadou for the practical assistance in using the VSP-G1. The authors express gratitude to Elekta for financial support of the project.

Conflict of interest

The authors declare that the research was conducted in the absence of any commercial or financial relationships that could be construed as a potential conflict of interest.

Generative AI statement

The author(s) declare that no Generative AI was used in the creation of this manuscript.

Any alternative text (alt text) provided alongside figures in this article has been generated by Frontiers with the support of artificial intelligence and reasonable efforts have been made to ensure accuracy, including review by the authors wherever possible. If you identify any issues, please contact us.

Publisher's note

All claims expressed in this article are solely those of the authors and do not necessarily represent those of their affiliated organizations, or those of the publisher, the editors and the reviewers. Any product that may be evaluated in this article, or claim that may be made by its manufacturer, is not guaranteed or endorsed by the publisher.

Supplementary material

The Supplementary Material for this article can be found online at: https://www.frontiersin.org/articles/10.3389/fnano.2025.1597129/full#supplementary-material

References

Burtscher, H., and Schmidt-Ott, A. (1982). Enormous enhancement of van der Waals forces between small silver particles. *Phys. Rev. Lett.* 48 (25), 1734–1737. doi:10.1103/physrevlett.48.1734

Cadavid-Rodriguez, M. C., Charvet, A., Bemer, D., and Thomas, D. (2014). Optimization of bubble column performance for nanoparticle collection. *J. Hazard Mat.* 271, 24–32. doi:10.1016/j.jhazmat.2014.01.040

Credence Research. Nanomedicine market size S, trends report 2024–2032. Available online at: https://www.credenceresearch.com/report/nanomedicine-market.

Dheyab, M. A., Aziz, A. A., Jameel, M. S., Noqta, O. A., Khaniabadi, P. M., and Mehrdel, B. (2020). Simple rapid stabilization method through citric acid modification for magnetite nanoparticles. *Sci. Rep.* 10 (1), 10793. doi:10.1038/s41598-020-67869-8

Didillon, B., Merlen, E., Pages, T., and Uzio, D. (1998). From colloidal particles to supported catalysts a comprehensive study of palladium oxide hydrosols deposited on alumina. *Stud. Surf. Sci. Catal.* 118, 41–54. doi:10.1016/s0167-2991(98)80166-3

Drdova, S., Gao, M., Sambalova, O., Pauer, R., Zhou, Z., Dimitriadou, S., et al. (2024). Precursor- and waste-free synthesis of spark-ablated nanoparticles with enhanced photocatalytic activity and stability towards airborne organic pollutant degradation. *Environ. Sci. Nano.* 11 (3), 1023–1043. doi:10.1039/d3en00348e

Feng, J., Huang, L., Ludvigsson, L., Messing, M. E., Maisser, A., Biskos, G., et al. (2016). General approach to the evolution of singlet nanoparticles from a rapidly quenched point source. *J. Phys. Chem. C* 120 (1), 621–630. doi:10.1021/acs.jpcc.5b06503

Fortin, J.-P., Wilhelm, C., Servais, J., Ménager, C., Bacri, J.-C., and Gazeau, F. (2007). Size-sorted anionic iron oxide nanomagnets as colloidal mediators for magnetic hyperthermia. *J. Am. Chem. Soc.* 129 (9), 2628–2635. doi:10.1021/ja067457e

Gaddis, E. S., and Vogelpohl, A. (1986). Bubble formation in quiescent liquids under constant flow conditions. *Chem. Eng. Sci.* 41 (1), 97–105. doi:10.1016/0009-2509(86)85202-2

Ghazi, R., Ibrahim, T. K., Nasir, J. A., Gai, S., Ali, G., Boukhris, I., et al. (2025). Iron oxide based magnetic nanoparticles for hyperthermia, MRI and drug delivery applications: a review. *RSC Adv.* 15 (15), 11587–11616. doi:10.1039/d5ra00728c

Grand View Research. Nanomedicine market size STARBM, by application, by indication, by region, and segment forecasts, 2024–2030. Available online at: https://www.grandviewresearch.com/horizon/outlook/nanomedicine-market-size/global.

Klencsár, Z. (1997). Mössbauer spectrum analysis by evolution algorithm. *Nucl. Instrum. Methods Phys. Res. Sect. B Beam Interact. Mater. Atoms* 129 (4), 527–533. doi:10.1016/s0168-583x(97)00314-5

Koch, D., and Weber, A. P. (2012). Separation of gas-borne nanoparticles in bubble columns. *J. Aerosol Sci.* 53, 61–75. doi:10.1016/j.jaerosci.2012.05.012

Laha, S. S., Thorat, N. D., Singh, G., Sathish, C. I., Yi, J., Dixit, A., et al. (2022). Rare-earth doped iron oxide nanostructures for cancer theranostics: magnetic hyperthermia and magnetic resonance imaging. *Small* 18 (11), 2104855. doi:10.1002/smll.202104855

Laurent, S., Dutz, S., Häfeli, U. O., and Mahmoudi, M. (2011). Magnetic fluid hyperthermia: focus on superparamagnetic iron oxide nanoparticles. *Adv. Colloid Interface Sci.* 166 (1), 8–23. doi:10.1016/j.cis.2011.04.003

Maier, A., Djanashvili, K., Denkova, A. G., van Rhoon, G. C., Pignol, J.-P., and van Oossanen, R. (2021). *Synthesis of hybride Palladium(103)/Iron oxide nanoparticles for thermobrachy therapy*. Hague, The Netherlands: European Patent Application.

Maier, A., van Oossanen, R., van Rhoon, G. C., Pignol, J.-P., Dugulan, I., Denkova, A. G., et al. (2022). From structure to function: understanding synthetic conditions in relation to magnetic properties of hybrid Pd/Fe-oxide nanoparticles. *Nanomaterials* 12 (20), 3649. doi:10.3390/nano12203649

Maier, A., Jia, Q., Shukla, K., Dugulan, A. I., Hagedoorn, P.-L., van Oossanen, R., et al. (2024). Enhancing magnetic hyperthermia efficiency in Pd/fe-oxide hybrid nanoparticles through Mn-Doping. *ACS Appl. Nano Mater.* 7 (23), 27465–27475. doi:10.1021/acsanm.4c05452

Maisser, A., Barmpounis, K., Attoui, M. B., Biskos, G., and Schmidt-Ott, A. (2015). Atomic cluster generation with an atmospheric pressure spark discharge generator. *Aerosol Sci. Technol.* 49 (10), 886–894. doi:10.1080/02786826.2015.1080812

Mathew, P., George, J., Mathews, T. S., and Kurian, P. J. (2019). Experimental verification of modified Paschen's law in DC glow discharge argon plasma. *AIP Adv.* 9 (2), 025215. doi:10.1063/1.5086246

Nedylakova, M., Medinger, J., Mirabello, G., and Lattuada, M. (2024). Iron oxide magnetic aggregates: aspects of synthesis, computational approaches and applications. *Adv. Colloid Interface Sci.* 323, 103056. doi:10.1016/j.cis.2023.103056

Nemati, Z., Alonso, J., Rodrigo, I., Das, R., Garaio, E., García, J. Á., et al. (2018). Improving the heating efficiency of iron oxide nanoparticles by tuning their shape and size. *J. Phys. Chem. C* 122 (4), 2367–2381. doi:10.1021/acs.jpcc.7b10528

Pellico, J., Ruiz-Cabello, J., and Herranz, F. (2023). Radiolabeled iron oxide nanomaterials for multimodal nuclear imaging and positive contrast magnetic resonance imaging (MRI): a review. *ACS Appl. Nano Mater.* 6 (22), 20523–20538. doi:10.1021/acsanm.3c04269

Pfeiffer, T. V., Feng, J., and Schmidt-Ott, A. (2014). New developments in spark production of nanoparticles. *Adv. Powder Technol.* 25 (1), 56–70. doi:10.1016/j.apt.2013.12.005

Reinmann, R., and Akram, M. (1997). Temporal investigation of a fast spark discharge in chemically inert gases. *J. Phys. D. Appl. Phys.* 30 (7), 1125–1134. doi:10.1088/0022-3727/30/7/010

Schwyn, S., Garwin, E., and Schmidt-Ott, A. (1988). Aerosol generation by spark discharge. *J. Aerosol Sci.* 19 (5), 639–642. doi:10.1016/0021-8502(88)90215-7

Simion, A. I., Grigoraş, C-G., and Gavrilă, L. G. (2014). Modelling of the thermophysical properties of citric acid aqueous solutions. Density and Viscosity. *Ann. Food Sci. Technol.* 15, 193–202.

Stanicki, D., Vangijzegem, T., Ternad, I., and Laurent, S. (2022). An update on the applications and characteristics of magnetic iron oxide nanoparticles for drug delivery. *Expert Opin. Drug Deliv.* 19, 321–335. doi:10.1080/17425247.2022.2047020

Starsich, F. H. L., Herrmann, I. K., and Pratsinis, S. E. (2019). Nanoparticles for biomedicine: coagulation during synthesis and applications. *Annu. Rev. Chem. Biomol. Eng.* 10, 155–174. doi:10.1146/annurev-chembioeng-060718-030203

Tabrizi, N. S., Ullmann, M., Vons, V. A., Lafont, U., and Schmidt-Ott, A. (2009). Generation of nanoparticles by spark discharge. *J. Nanopart Res.* 11 (2), 315–332. doi:10.1007/s11051-008-9407-y

Tabrizi, N. S., Xu, Q., van der Pers, N. M., and Schmidt-Ott, A. (2010). Generation of mixed metallic nanoparticles from immiscible metals by spark discharge. *J. Nanopart Res.* 12 (1), 247–259. doi:10.1007/s11051-009-9603-4

Vangijzegem, T., Lecomte, V., Ternad, I., Van Leuven, L., Muller, R. N., Stanicki, D., et al. (2023). Superparamagnetic iron oxide nanoparticles (SPION): from fundamentals to state-of-the-art innovative applications for cancer therapy. *Pharmaceutics* 15 (1), 236. doi:10.3390/pharmaceutics15010236

Walter, A., Garofalo, A., Parat, A., Martinez, H., Felder-Flesch, D., and Begin-Colin, S. (2015). Functionalization strategies and dendronization of iron oxide nanoparticles. *Nanotechnol. Rev.* 4 (6), 581–593. doi:10.1515/ntrev-2015-0014

Winkler, R., Ciria, M., Ahmad, M., Plank, H., and Marcuello, C. (2023). A review of the current state of magnetic force microscopy to unravel the magnetic properties of nanomaterials applied in biological systems and future directions for quantum technologies. *Nanomaterials* 13 (18), 2585. doi:10.3390/nano13182585

Zhang, S. L., and Zhang, J. R. (1994). Photoemission and mössbauer effect studies of sputter-deposited fe-pd alloys. *Phys. status solidi (b)* 182 (2), 421–427. doi:10.1002/pssb.2221820219